

Elastic and Plastic Characteristics of Sodium Metal

Cole D. Fincher, Yuwei Zhang, George M. Pharr, and Matt Pharr*

Cite This: *ACS Appl. Energy Mater.* 2020, 3, 1759–1767

Read Online

ACCESS |



Metrics & More



Article Recommendations



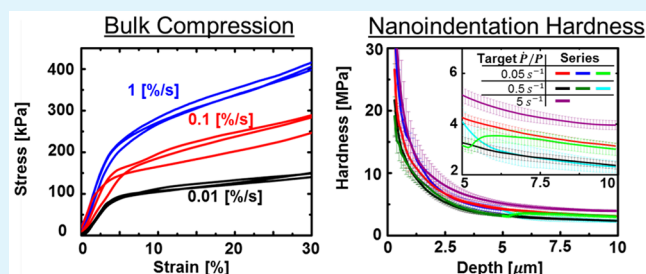
Supporting Information

ABSTRACT: Sodium metal holds promise as an anode material for rechargeable batteries due to its large theoretical charging capacity, low electrochemical potential, earth abundance, and low cost. However, a number of concerns remain that must be addressed prior to practical implementation, particularly Na's propensity to form unstable morphologies during electrochemical deposition. Given the importance of mechanical deformation in this process, unlocking the potential of sodium metal as an anode material requires a thorough understanding of its mechanical properties. To this end, we evaluate the mechanical properties of sodium metal at room temperature through a combination of bulk compression, microhardness, and nanoindentation tests. With regard to elastic properties, nanoindentation testing produced an elastic modulus of 3.9 ± 0.5 GPa. With regard to plastic properties, bulk compression testing revealed the flow stress at 0.08 strain as varying between 102 and 254 kPa at strain rates between 10^{-4} and 10^{-2} s^{-1} . Nanoindentation indicated a decrease in hardness from 26.6 to 2.3 MPa at target $\dot{P}/P = 0.05 \text{ s}^{-1}$ as the indentation depth increased from 0.25 to 10 μm , while microhardness testing indicated hardness values between 1.6 and 1.1 MPa at depths varying between 50 and 130 μm . We perform finite element simulations to relate length scales in these measurements (e.g., depth) to physical lengths scales relevant to battery applications. We also found that Na exhibits a marked strain-rate sensitivity, with a strain-rate sensitivity exponent of $m = 0.14$ from nanoindentation and $m = 0.20$ from bulk compression. Likewise, indentation demonstrated that Na is even more susceptible to creep than is Li metal. Overall, our studies indicate that Na metal is extremely soft, readily creeps, and exhibits pronounced size effects. We discuss the implications of these properties relative to other candidate anode materials of rechargeable batteries. Most notably, Na's greater propensity to creep than Li, in turn, has implications for charging rate capability in solid-state batteries.

KEYWORDS: metal anode, plasticity, yield strength, elastic modulus, sodium, creep, hardness, mechanical properties, battery

INTRODUCTION

Sodium-based batteries have garnered recent attention largely due to Na's abundance, low cost, and limited geographic constraints.^{1,2} As such, they may find applications where Li-based batteries are not as viable, such as in grid-scale energy storage from renewable resources.³ Additionally, unlike Li, Na's inability to alloy with Al enables pairing Na metal anodes with Al current collectors, as compared to the heavier and commonly used Cu current collectors, thereby simplifying the manufacturing process and reducing manufacturing costs by an estimated 8%.^{4,5} Of potential candidates for anodes in sodium-ion systems, sodium metal itself has the lowest electrochemical potential (-2.71 V vs the standard hydrogen electrode) and the highest theoretical capacity (1165 mAh/g).^{1,2} However, growth of Na dendrites can produce short circuits and induce explosion hazards.^{1,6,7} In fact, a recent study suggests that Na metal electrodes are even more prone to dendritic growth than are those of Li.⁸ Additionally, reduction of most electrolytes occurs readily at Na's surface, producing a solid electrolyte interphase (SEI), which consumes active material.^{1,9,10} Finally, Na metals suffers from so-called "infinite volume change" due to its hostless nature (i.e., it involves a plating process).⁶



Cycling exacerbates degradation, ultimately resulting in capacity fading and safety hazards that must be addressed prior to practical implementation.^{9,11,12}

The mechanical properties of the Na metal anode play a key role in the cyclability of the battery.^{13–16} For metallic anodes in liquid electrolyte systems, mechanical pulverization and capacity loss remain significant challenges, largely due to dendritic/nonuniform growth during electrochemical deposition.¹⁷ Likewise, loss of contact during cycling at the interface between a solid-state electrolyte (SSE) and the metallic electrode continues to stymie development of solid-state batteries.^{18–22} For such systems, the mechanical properties (i.e., yield stress, elastic modulus, and time-dependent plasticity) dictate the stress sustained by the electrode (and the surrounding electrolyte) under various geometries and loading conditions, e.g., at different charging rates. The stresses

Received: November 13, 2019

Accepted: January 23, 2020

Published: January 23, 2020



in turn may affect the electrode kinetics (by modifying the total electrochemical potential of the electrode),^{23–26} the growth morphology under cycling,^{23,27} and/or the integrity of the contact at the anode/SSE interface.^{28–30} Progress regarding solid-state Na batteries appears encouraging.^{18,31–33} However, the recent study by Spencer Jolly et al. indicates that creep of Na is a crucial process in overcoming void formation at the SSE/anode interface, thereby averting cell death.³⁰ Strategies to mitigate these cycling issues will require a thorough understanding of Na's mechanical properties.

Despite the importance of Na's mechanical properties, surprisingly little is known. A few studies^{34–38} have presented single crystal elastic constants of Na at a variety of temperatures (see Table 1). However, no studies have probed

Table 1. Single Crystal Elastic Constants of Na Metal Measured through the Ultrasonic Pulse Echo Technique along with the Calculated Lower and Upper Bounds on the Elastic Modulus As Predicted by Hashin and Shtrikman⁵¹

ref no.	C11 (GPa)	C12 (GPa)	C44 (GPa)	temp (K)	E_{lower} (GPa)	E_{upper} (GPa)
34	5.34	2.31	2.04	200	4.59	4.60
35	7.39	6.22	4.19	299	4.56	6.08
36	8.21	6.83	5.77	78	5.62	7.92
	8.03	6.70	5.53	115	5.41	7.62
	7.83	6.53	5.27	155	5.25	7.32
	7.66	6.40	5.00	195	5.06	7.00
37	8.10	6.80	5.10	300	5.22	7.19
38	7.71	6.30	4.42	300	5.17	6.55

the elastic properties of aggregate (polycrystalline) sodium metal. Even more pressing is the lack of knowledge of Na's plastic properties. More than a century ago, Edwards investigated the resistance of bulk Na using Brinell style tests, reporting a hardness number of 0.07.³⁹ However, these samples were likely contaminated due to air exposure during testing. In addition, Herke, Kirchner, and Schoeck present stress–strain curves of Na in tension at various temperatures, but no strain rate is explicitly stated.⁴⁰ Furthermore, the plot units are not clearly defined, but the trend presented appears to show that the critical resolved shear stress was approximately constant between 200 and 300 K.⁴⁰ Lastly, Sargent and Ashby⁴¹ conduct creep tests at room temperature but do not present other important mechanical information (such as stress–strain curves).

Given this relative dearth of information, herein we detail mechanical properties of sodium metal at room temperature. Through nanoindentation, we quantify elastic properties of Na metal. By combining nanoindentation with microhardness testing and bulk compression tests, we characterize Na's plastic response across multiple length and time scales. We compare the mechanical characteristics of Na with those of other candidate metallic anodes of rechargeable batteries. Finally, we discuss practical implications of this work, with an eye toward battery scientists and designers.

METHODS

Sample Preparation. The condition of as-received sodium metal (Sigma-Aldrich, 99.9% purity cubes) poses challenges to indentation and tensile testing due to both the initial geometry (a cube with ~1 cm edge length) and because the surface is often covered with a thin purple film layer. In an attempt to mitigate effects of sample contamination, all samples were prepared in an argon glovebox

possessing less than 0.1 ppm of O₂ and H₂O. Oil (Sonneborn PD-28 highly refined white mineral oil) used for sample preparation was stored in the glovebox with 3 Å molecular sieve to remove moisture inside the container for more than 1 month prior to use.⁴² The as-received grain size appeared to be near 450 ± 220 μm based upon the linear intercept technique.

For indentation testing, the sodium cube was sectioned by using a new razor blade to reveal a shiny and pristine surface. Mineral oil was immediately applied to the exposed surface after sectioning. The backside of the sample was then adhered to a nanoindentation mount with Loctite gel adhesive. The mounted sample was placed between two well-oiled borosilicate glass plates. These plates were placed inside a hydraulic crimper and pressed to flatten the sample. The sample and indentation mount were immediately removed and mounted on the nanoindenter (also within the glovebox). All data within this study were collected within 3 h of sample preparation.

Nanoindentation Methods. Nanoindentation measurements of hardness, H , and elastic modulus, E , were made using a Nano-mechanics Nanoflip nanoindenter operated in the glovebox with less than 0.1 ppm of O₂ and H₂O (filled with argon gas from Praxair, 99.999% purity). All measurements were made with a Berkovich triangular pyramid indenter using the continuous stiffness measurement technique (CSM) at a frequency of 110 Hz with a target root-mean-square (rms) amplitude of 1 nm.^{43,44}

While precise knowledge of the indenter area function can typically be gathered from a fused silica calibration standard, the studies herein require measurements at much larger depths than can be easily achieved in fused silica. Thus, the fused silica area function was supplemented by measurements of data from polycarbonate (Makrolon, 0.08 in. thickness, ASTM D3935 class 1 polycarbonate sheet) in a manner similar to that described by Ginder and Pharr.⁴⁵ This area function was calibrated over the range of 300 nm–10 μm; as such, nanoindentation measurements outside of this range are not presented.

Indentation of Na requires considerations of indentation pile up due to its extremely high E/H ratio. Optical imaging of the contact area from nanoindentation tests (indented with target $\dot{P}/P = 0.05/s$) revealed that the contact depth was ~1.06 times the measured indenter penetration depth. Thus, in calculating the measured contact area A_c for this work, the reported contact depth was taken as 1.06 times the measured contact depth. We note that the degree of pileup should depend on the E/H ratio of a material, and thus the accuracy of the pileup assumption (that $h_c/h = 1.06$) should vary with depth for a material with depth-dependent hardness.⁴⁶ Additionally, a convenience afforded by Na's high E/H ratio is that very little elastic recovery occurs during unloading (the depth recovery is less than 1% of the total penetration depth). Thus, for hardness measurements, we can discard the typical sink-in correction to contact depth, rendering the hardness measurement independent of the measured contact stiffness. In all tests, the point of contact was initially identified based upon a 250 nm/s approach rate using a change of dP/dh of 100 N/m with data acquisition at 220 Hz. The point of contact was more accurately identified by visual inspection of the data after the test, with the estimation reflecting the point of contact to within 20 nm or better in depth.

Microhardness Testing. The same samples used for nanoindentation were also used for microhardness testing. After nanoindentation testing was complete, the sample and mount were submerged in mineral oil before removal from the glovebox to mitigate potential effects from air exposure. During transport, a glass slide was used to cover the surface of the sample while submerged in oil. Microhardness testing was conducted on the sample through 1 in. of oil using a Wilson TUKON 1102 microhardness tester with a Vickers tip. The loading to maximum force occurred over 5 s, followed by a prescribed dwell time at the maximum load. 20, 7, and 7 indents were conducted at maximum loads of 10g, 25g, and 50g force, respectively, all with a 10 s dwell time at the maximum applied load. Subsequent optical imaging of the sample through oil and the glass slide enabled observation of the contact area of the microhardness indents as well as validation of the ultimate contact area from

nanoindentation. The presented microhardness results represent the Meyer hardness or the force divided by the projected area (as measured from optical microscopy). The corresponding microhardness indentation depth referenced within the Results section was then estimated by approximating the indenter as having an ideal area function ($A_c = 24.5h_c^2$).

Bulk Compression Testing. For bulk tests, sodium cubes were cut within the glovebox into prisms with a rectangular cross sections possessing a width-to-height ratio of ~ 1.6 (width of 6 ± 1.2 mm, height of 10.5 ± 1.1 mm). After preparation, the cubes were measured with calipers and then stored under oil within the glovebox. Just before testing, the cubes were transferred to an oil bath and then removed from the glovebox (see Figure S1 for an example specimen). An Instron 5943 testing system was used to perform compression tests through the oil bath immediately upon removal from the glovebox. The samples were not observed to change color between removal from the glovebox and the conclusion of mechanical testing, thereby suggesting minimal effects of contamination.

Finite Element Analysis. Finite element analysis provided insight into the physical length scales probed by the nanoindentation measurements. The axisymmetric simulation presented in Figure 1

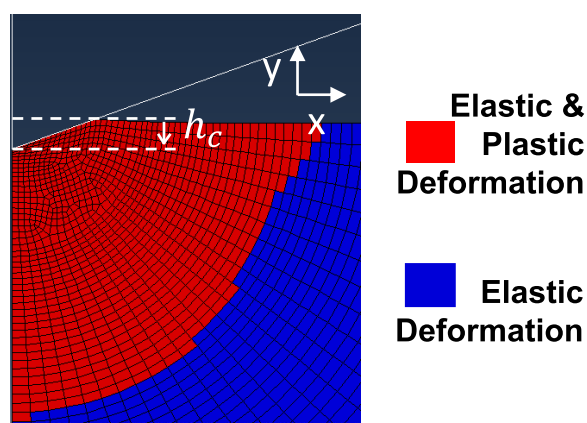


Figure 1. Actively yielding elements (AC_Yield output) from ABAQUS used to estimate the volume of the plastic zone under the indenter for nanoindentation experiments. The red region represents the elements undergoing plastic and elastic deformation, while the blue region undergoes elastic deformation only.

consisted of an analytical rigid surface (the indenter) possessing an internal angle of 70.2° (the cone angle with the same self-similar contact area with respect to depth as a Berkovich indenter tip) in contact with a solid mesh of 4 node axisymmetric elements (CAX4R) elements. Nonlinear geometric effects were included, and the elastic behavior of the solid was defined with an elastic modulus of 3.5 GPa and a Poisson's ratio of 0.3. The plastic flow stress was defined as a function of plastic strain by inputting the stress–strain data from an experimentally measured sodium compression stress–strain curve (for bulk compression to 0.3 strain at a strain rate of 10^{-3} s^{-1}). The indenter in the simulation was specified to have x displacement, z displacement, and all rotations fixed at zero ($U1 = U3 = UR2 = UR3 = UR1 = 0$), with the indenter tip displaced downward into the solid (i.e., $U2 = -h_c$). The solid was defined as having a fixed boundary on the bottom-most surface with the left side possessing a y -axis symmetric boundary condition. A finite-sliding interaction was defined between the indenter and solid surface, using surface-to-surface discretization and adjustment only to remove overclosure. This interaction was defined to have frictionless tangential behavior. For the input flow stresses, the simulations produced a plastic volume which (if treated as scaling like a hemisphere) possesses a radius of $11.1h_c$. Meanwhile, the von Mises stress decays to below 1% of the maximum value at a depth of $40.5h_c$.

RESULTS

Elastic Modulus. Figure 2 displays indentation measurements of Na conducted within 1 h of sample preparation. Each

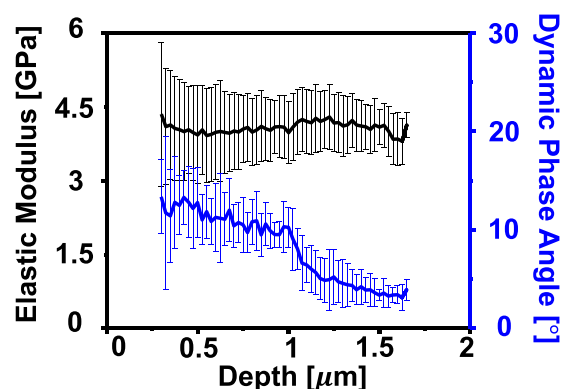


Figure 2. Elastic modulus and corresponding dynamic phase angle from 10 nanoindentation tests in Na. All tests were performed within 1 h after surface preparation. The indents were conducted using a target loading rate divided by load of $\dot{P}/P = 0.05$ [1/s] to a depth of $1 \mu\text{m}$, followed by a 60 s constant load hold.

curve represents the average of 10 tests, with the error bars spanning one standard deviation from the mean. These tests used a target $\dot{P}/P = 0.05/\text{s}$ loading scheme to a target depth of $1 \mu\text{m}$, followed by a constant load hold for 60 s. Additional information regarding this test set, such as individual load–depth curves and the indentation strain rate, is provided in the Supporting Information (Figure S2). As noted by Merle, in a material with a large E/H ratio, a high dynamic phase angle (e.g., 10° or higher) may reflect the encroachment of plastic deformation upon the dynamic displacement oscillation used for the continuous stiffness measurement.⁴⁷ We note that the dynamic phase flattens out at a relatively small dynamic phase angle (near a few degrees) as the load hold begins at the $1 \mu\text{m}$ indentation depth, implying that plasticity error can be treated as negligible for depths larger than $1 \mu\text{m}$. Because the elastic modulus does not appear to change significantly with depth, this sample does not seem to exhibit any effects of a surface film. As such, the elastic modulus observed during the load hold (3.9 ± 0.5 GPa) likely represents that of polycrystalline Na metal, i.e., the form typically used in battery applications.

Nanoindentation Hardness. Figure 3 shows the measured nanoindentation hardness of Na metal. Each curve represents the average of seven tests. Individual indentation tests were placed randomly in the samples by moving >2 mm between each indent. The error bars represent the standard deviations in the measured values at the corresponding depth. All data are plotted for depths of $0.3 \mu\text{m}$ (the lower bound for area function calibration) and larger. Plots of the loading rate by load vs depth as well as the individual indentation load–depth curves, indentation strain rates vs depth, and hardness vs depth can be found in Figures S3–S8.

From Figure 3A, the hardness decreases significantly with depth before approaching a relatively constant value for the three tests conducted at a constant \dot{P}/P (black, red, and violet curves). While this decrease in hardness suggests an indentation size effect,^{48,49} some variation may also arise from changes in strain rate (as seen in Figure 3B) during the test. Additionally, while no direct evidence of a surface film exists, its presence cannot completely be ruled out. To

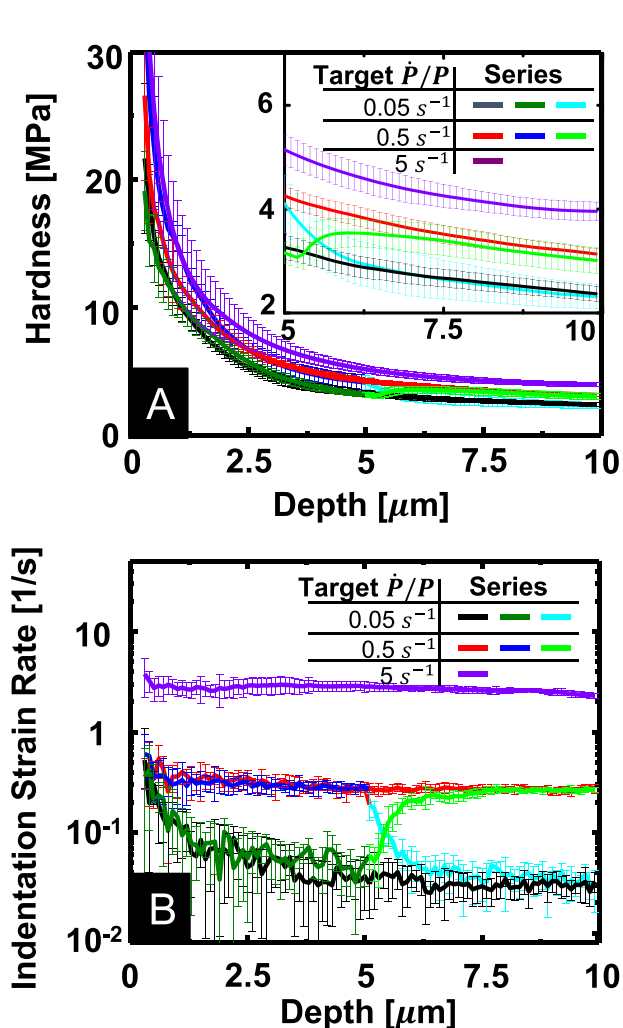


Figure 3. Nanoindentation tests, with each series representing the average of seven or more individual indents conducted under identical test conditions. (A) The indentation hardness and (B) the indentation strain rate (dimensionally, \dot{h}/h). Scatter bars span one standard deviation from the mean. All corresponding load–depth curves can be found in the Supporting Information.

determine whether history effects occurred, we implemented tests in which the target indentation strain rate was changed at a specified depth. Namely, in Figure 3A, the blue curve jumps from a target $\dot{P}/P = 0.5/s$ to $0.05/s$, while the green curve jumps from $\dot{P}/P = 0.05/s$ to $0.5/s$ at a depth of $5 \mu\text{m}$. After brief transients following the jump, the indentation strain rates and hardnesses both recover to the hardnesses of the corresponding constant \dot{P}/P tests, which indicates that Na's hardness is relatively history-independent under the tested conditions.

Because Na is relatively history independent and the strain rates approach a constant value, we attribute the difference in hardness among the three hardness at constant target \dot{P}/P (black red, and violet curves) to the rate-dependent plasticity of Na metal. Fitting the indentation strain rate (\dot{h}/h) and hardness at a depth of $10 \mu\text{m}$ to the relationship $H = \kappa \left(\frac{\dot{h}}{h}\right)^m$ produces a strain-rate sensitivity exponent of $m = 0.138$, with a coefficient of $\kappa = 3.59 \text{ MPa}\cdot\text{s}^m$, as seen in Figure 4.

Bulk Compression. Figure 5 displays the engineering stress–strain response for compression testing of bulk sodium.

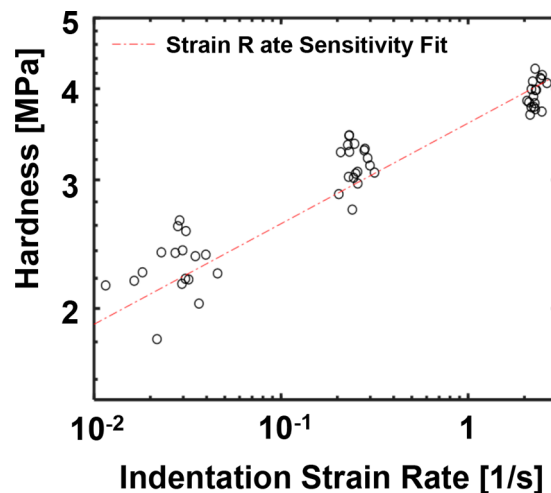


Figure 4. Indentation hardness versus indentation strain rate ($\frac{\dot{h}}{h}$) measured at $10 \mu\text{m}$ indentation depths for constant target $\frac{\dot{P}}{P}$ tests shown in Figure 3. The strain-rate sensitivity fit follows the form of $H = \kappa \left(\frac{\dot{h}}{h}\right)^m$, where $\kappa = 3.59 \text{ MPa}\cdot\text{s}^m$ and $m = 0.138$.

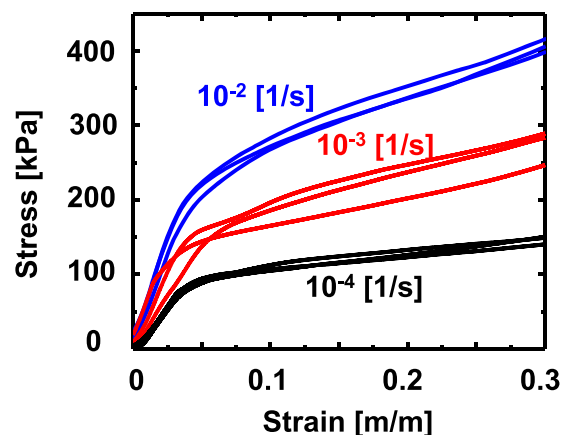


Figure 5. Stress–strain relationship for Na under bulk compression at several loading rates with blue lines for 0.01 1/s , red for 0.001 1/s , and black for 0.0001 1/s .

The upper limit on the horizontal axis was chosen to omit data with testing artifacts associated with sample barreling at strains higher than 0.3 (as seen in Figure S9). While some fluctuations occur at low stress and strain values, perhaps due to slight misalignment between the sample surface and the compression platen, the stress–strain curves appear to be approximately linear at strains larger than 0.05 strain. At strains of 0.08 , the measured flow stresses were 102 ± 2.3 , 170 ± 12 , and $254 \pm 9.1 \text{ kPa}$ at loading rates of 10^{-4} , 10^{-3} , and 10^{-2} 1/s , respectively, thereby indicating a significant rate dependence. Fitting the measured stress values at a specified strain (taken as $\epsilon = 0.08$) within this region to the relation $\sigma = \kappa \dot{\epsilon}^m$ gives a strain-rate sensitivity exponent of $m = 0.20$ with the coefficient $\kappa = 0.64 \text{ MPa}\cdot\text{s}^m$, as seen in Figure 6.

Microhardness. Microhardness testing further attests to the soft nature of Na. Indents with loads at 10 , 25 , and $50 \text{ gram-force (gf)}$ with a 10 s dwell time at the maximum load produced hardnesses of 1.6 ± 0.05 , 1.2 ± 0.08 , and $1.1 \pm 0.09 \text{ MPa}$, respectively (mean \pm standard deviation). Assuming that

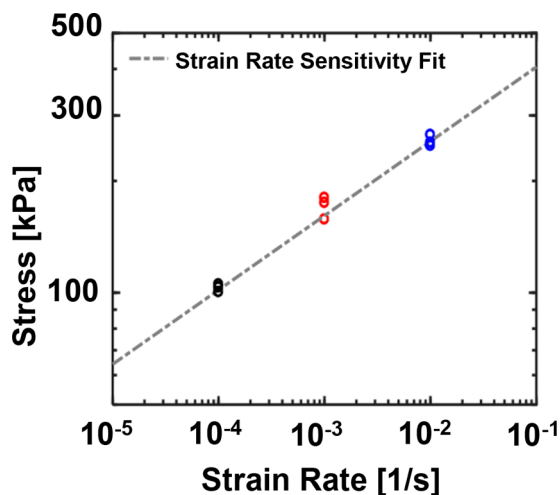


Figure 6. Strain rate vs the flow stress measured stress at 0.08 strain for bulk compression tests of sodium. The trend line represents the fit for strain-rate sensitivity following $\sigma = \kappa \dot{\epsilon}^m$, where $\kappa = 0.64 \text{ MPa}\cdot\text{s}^m$ and $m = 0.20$.

the indenter area function is ideal, the hardness measurements for the 10, 25, and 50 gf indents correspond to ultimate indentation depths of 50 ± 1 , 91 ± 3 , and $135 \pm 5 \mu\text{m}$, respectively. Indents conducted at 10 gf with a 60 s dwell time produced hardness measurements of $1.05 \pm 0.06 \text{ MPa}$ at ultimate depths of $60 \pm 2 \mu\text{m}$ (as compared $1.6 \pm 0.05 \text{ MPa}$ measured by using the same load but with a 10 s dwell time), thereby further attesting to the presence of rate-dependent plasticity.

Comparison with Lithium Metal. Figure 7A presents four indentation load–depth curves for both lithium and sodium, prepared and tested in identical fashions. The lithium data are taken from a recent study by Fincher et al.⁵⁰ For both materials, a target $\frac{\dot{P}}{P} = 0.05/\text{s}$ was used during the loading segment, up to a depth of $5 \mu\text{m}$. Figure 7B shows that the indentation strain rates for both sets of experiments were similar during the loading period. Following the loading segment, the maximum load was held for a period of 30 min, allowing the indenter tip to creep deeper into the sample. On average, the indenter crept forward $3.6 \mu\text{m}$ during the load hold for sodium indents, as compared to the $2.1 \mu\text{m}$ for the lithium indents. Overall, these tests indicate that Na is significantly softer and creeps significantly faster than Li.

DISCUSSION

Elastic Properties of Sodium. A few previous studies have experimentally measured single crystal elastic constants of Na at varying temperatures using the ultrasonic pulse echo technique, as seen in Table 1. E_{upper} and E_{lower} correspond to bounds on the aggregate elastic modulus as calculated by the Hashin and Shtrikman analysis using the corresponding single crystal elastic constants.⁵¹ Our nanoindentation measurements of the elastic modulus ($3.9 \pm 0.5 \text{ GPa}$) are slightly lower than the predicted aggregate elastic modulus based on the application of the Hashin and Shtrikman model to the previous measurements (Table 1). We argue that the most likely potential sources of experimental error have been eliminated: the area has been verified by optical microscopy, while the phase angle data indicate that any “plasticity error” is minimal. One potential explanation for this discrepancy is that

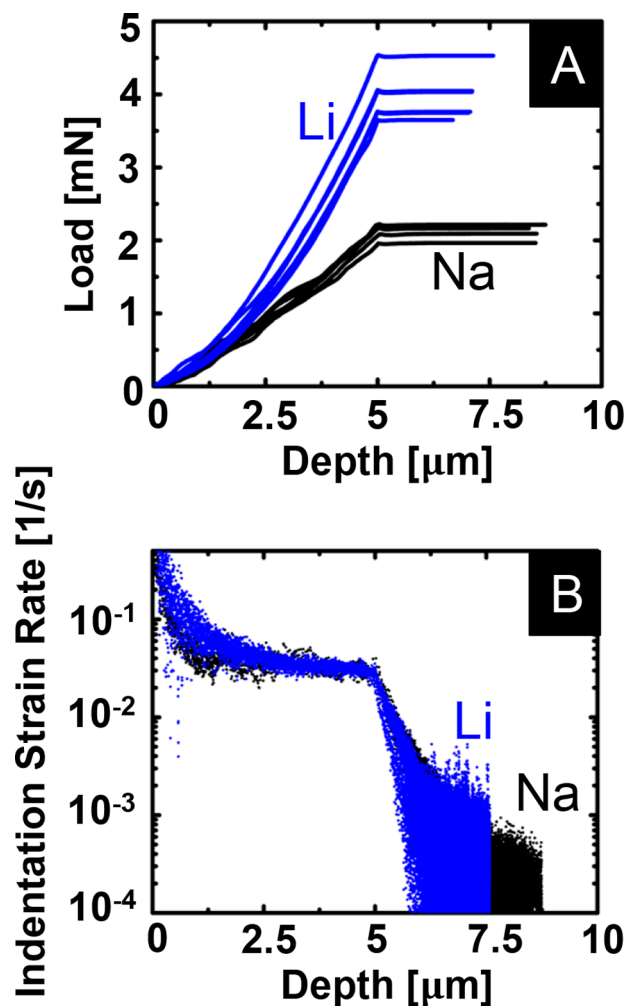


Figure 7. (A) Indentation load–depth curves on both lithium from Fincher et al.⁵⁰ and sodium metal. (B) Indentation strain rate (\dot{h}/h) vs depth, conducted at a target $\dot{P}/P = 0.05/\text{s}$ to a depth of $5 \mu\text{m}$, followed by a 30 min load hold. The indenter tip drifts forward $\sim 70\%$ farther during the load hold for the sodium as compared to the lithium, despite the sodium hold occurring at a lower load.

the sodium that we tested may possess some preferred crystal texture. This texture may affect the measured elastic modulus if the size of the elastically deformed zone is on the same order as the grain size. Still, despite being slightly smaller, our measured value of Na’s elastic modulus is similar in magnitude to Hashin and Shtrikman estimations based on measured single crystal elastic constants in the literature.

When considering other candidate metallic anode materials for rechargeable batteries (e.g., Li and Mg which possess elastic moduli near 9.4 GPa ⁵⁰ and 40 GPa ,⁵² respectively, as measured from similar nanoindentation), Na appears to possess a significantly lower elastic modulus (3.9 GPa) based on our nanoindentation results. The Newman and Monroe model, a popular model for describing the stability of the electrode–separator interface, predicts (using only linear elasticity) that implementing a separator with twice the shear modulus of the anode will prevent unstable and dendritic growth.²⁷ While this model does have significant limitations (e.g., not accounting for plastic deformation), it suggests that Na’s low elastic modulus may assist in enhancing the stability of the separator–electrode interface (e.g., preventing metallic dendrite formation), at least under elastic loading.

Plastic Properties of Sodium. Figure 8 shows the measured equivalent flow stress of Na as a function of length

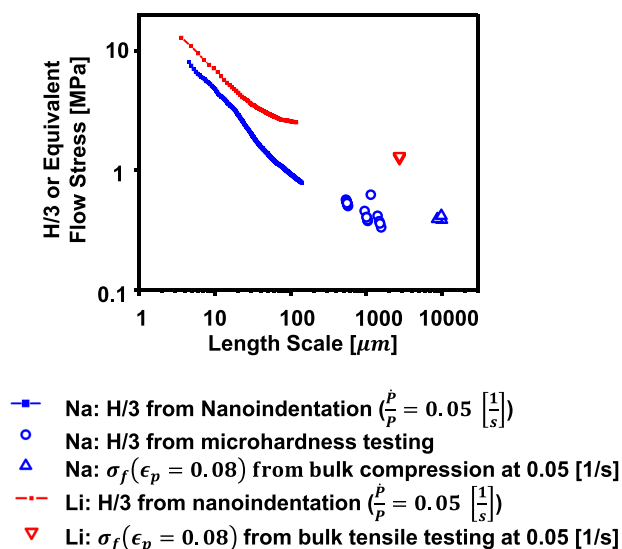


Figure 8. σ_f or $H/3$ plotted vs representative length scale, with the blue series representing Na data from this study and the red data representing Li data from the previous study of Fincher et al.⁵⁰

scale for the bulk compression, microhardness, and nanoindentation tests provided in this study. In relating the nanoindentation and microhardness tests to an equivalent flow stress, we take the Tabor relation as $\sigma_f \cong H/3$. Previous studies of metals have shown that in this relation the $H/3$ value from a Vickers or Berkovich tip geometry correlates with the flow stress at an equivalent strain of $\cong 0.08$ from a uniaxial test.⁵³ Uniaxial compression curves for 0.05 1/s rate can be seen in Figure S9. We note that Figure 8 does not account for the varied strain rates present in the different test methods (because there is no direct conversion from indentation strain rate to bulk uniaxial compression strain rate, and thus the indentation strain rate and uniaxial strain rate are not strictly the same). However, we note that the nanoindentation measurements and the bulk compression experiments each show that the measured hardness or flow stresses vary by less than a factor of 3 at strain rates varying by over 2 orders of magnitude (as seen in Figures 3 and 6). Although significant, this variation is small compared to the variation in equivalent flow stress with length scale, as observed in Figure 8. Also, in constructing Figure 8, we argue that the length scale most appropriate for comparing the hardness among the various tests is the size of the plastic zone during the test. Thus, we use the equivalent plastic zone radius (11.1 times the indentation depth, as determined from finite element simulations; Figure 1) for the length scale associated with the nanoindentation and microhardness tests. For the bulk tests, we use the square root of the cross-sectional area as the characteristic length.

The equivalent flow stress of Na from nanoindentation (from $\dot{\epsilon} = 0.05/\text{s}$) decreases from ~ 8 MPa to nearly 0.8 MPa as the characteristic length scale increases from 4.5 to 140 μm . The microhardness continues with a similar trend, decreasing from 560 to nearly 330 kPa as the length scale increases from 680 to 1950 μm . Finally, the bulk compression tests produce a flow stress of 190 kPa at a characteristic length scale near 10000 μm .

Implications for Na Batteries. Metallic lithium has been widely studied from an electrochemical perspective as a candidate anode material because of a number of excellent electrochemical characteristics; namely, it has the largest theoretical capacity of all anode materials. Figure 8 shows the data from Fincher et al.⁵⁰ for Li metal under equivalent testing conditions to the Na presented in this study. Comparing these two materials in terms of mechanical properties, Figure 8 indicates that Na is significantly softer than Li. In addition, Figure 7A indicates that Na creeps more readily than Li, as may be expected due to Na's lower melting point (~ 98 °C for Na and 180 °C for Li) and thus higher homologous temperature ($0.8T_m$ for Na and $0.65T_m$ for Li during the room temperature tests). Additionally, the bulk tests herein can be compared with previous studies of Li for further insight. The strain-rate sensitivity exponent of $m = 0.20$ (measured in this study) can be written as a stress exponent of $n = 5$ (for the equation $\dot{\epsilon} = A\sigma^n$), a value lower than the stress exponent measured for Li in various studies ($n = 6.56$,⁵⁴ $n = 6.6$,⁵⁵ and $n = 6.55$ ⁵⁰). This comparatively low stress exponent from bulk tests only further indicates that Na is more prone to creep than Li.

These observations of sodium's soft nature have key implications in potential applications as metallic anodes. Because of Na being soft compared to Li, Na dendrites may have a greater propensity to blunt (i.e., flatten out) rather than puncture battery separators or solid electrolytes during solid-to-solid contact. Future experiments should seek to compare the mechanics of Li and Na metal during battery operation. Additionally, less externally applied pressure may be required to prevent the formation of Kirkendall voids (as compared to the pressures observed for formation in Li).⁵⁶ Furthermore, fracture of the solid electrolyte interphase (SEI) remains a significant source of degradation and capacity fade of metallic batteries.^{57,58} Although relatively little is known regarding surface films on sodium, SEI layers tend to be relatively stiff. As such, sodium's soft nature likely leads to a large mismatch in mechanical properties at the SEI/electrode interface, which may have implications for electrode reversibility (e.g., through fracture, delamination, or otherwise degrading the SEI layers).^{9,57,58}

Additionally, the strain-rate-sensitive response of Na has implications in practical battery systems. In a battery system, the charging rate may be viewed as related to an applied strain rate; i.e., faster charging produces higher strain rates. Thus, the measured strain-rate dependence of Na implies that dendrites may have larger strengths under faster charging rates. Furthermore, several studies of Li anodes suggest a relationship between charging rate and dendrite morphology, which may be at least partially attributable to strain-rate effects.^{59,60} While at least one recent study suggests that similar morphological transitions are present in Na,⁶¹ the importance of such rate dependence in the Na system (and the influence of Na's rate-dependent plasticity) requires future study.

The observed size dependence of hardness (Figures 3 and 8) also has implications in practical systems. In general, for defects at the SSE/anode interface, the size dependence of Na's hardness may lead to stress relaxation or intensification depending on the defect size in a manner similar to that discussed by Herbert et al. in the context of Li.⁶² Furthermore, dendrites initiate at small radii (likely at the nanometers scale) and grow to different sizes and shapes depending on the cell conditions.^{63–68} As such, the results in Figure 8 suggest that

the mechanical properties of a Na electrodeposit will continuously evolve during nucleation and growth. These changes in mechanical properties during growth may influence the level of sustained stress in both the electrodeposit and the surrounding solids as well as the subsequent morphological stability of the electrodeposit. For instance, if the electrodeposit becomes softer as it grows, a solid-state electrolyte or stiff separator may be strong enough to prevent dendritic penetration (in a manner similar to the Newman and Monroe model as discussed above). Overall, the results in Figure 8 suggest a pronounced size effect of the plastic properties of sodium, which warrants future microstructural studies aimed at determining deformation mechanisms.

The formation and propagation of defects in SSE's remains a significant additional challenge for solid-state batteries. As potential disadvantage, Na's propensity for creep may lead to undesired deformation when subjected to static loads, e.g., so-called "stack pressure" in packaged batteries. To this end, the ability to readily flow/creep may facilitate transport of Na toward the cathode through grain boundaries in solid electrolytes, as has been observed in the Li system, which again warrant future studies.^{69,70} Furthermore, the enlarged size of the Na ion as compared to the Li ion (cation radius of 97 Å vs 68 Å, respectively⁷¹) may also result in more strain within the SSE during operation. At the same time, Na's low elastic modulus and relative softness may result in reduced stresses at the SSE/anode interface, reducing the propensity of SSE's to fracture.

For solid-state batteries, interfacial contact (aka "interfacial wettability") between metallic anodes and the solid electrolyte remains a significant challenge. Some studies use a "press and pray" approach, introducing stack pressure and occasionally heat during assembly to establish "interfacial wettability."^{31,72–74} Still, loss of ionic contact may occur during cycling for a variety of reasons, e.g., the formation of ionically blocking layers due to side reactions, the loss of physical contact due to volume change of the electrode, or void formation due to stripping at the interface.^{31,74–76} However, the soft nature of Na may endow Na metal batteries with more conformal contact (as compared to Li and Mg) under pressure due to its facile deformation. Thus, Na's soft nature and propensity to creep may act as a boon toward establishing interfacial contact in solid-state batteries. In fact, recent studies from Bay et al.⁷⁶ and Wang et al.⁷⁷ demonstrate that the critical current densities for dendrite formation were approximately ten times higher for Na metal cycled across Na-β"-alumina as compared to Li metal cycled across garnet-type LLZO under similar conditions. Bay et al.⁷⁶ attribute the comparatively high critical current density for the Na / Na-β"-alumina battery to the "diffusive and mechanical properties of the alkali metal and solid-electrolyte." Furthermore, recent studies from Kasemchainan et al.²⁹ and Spencer Jolly et al.³⁰ indicate that creep plays the dominant role in maintaining interfacial contact in solid-state batteries. By comparing two recent studies, Kasemchainan²⁹ noted that Na metal could be cycled at higher current density than Li metal while maintaining interfacial contact, likely due to Na exhibiting greater creep.^{29,30} Toward this end, our study confirms that Na's creep is significantly more pronounced than Li. This finding only further indicates that Na metal should be capable of being cycled at higher current densities than Li metal while maintaining interfacial contact.

CONCLUSIONS

In this study, we have quantified elastic and plastic properties of sodium metal at room temperature. Overall, the studies show that Na metal is extremely soft and compliant, readily creeps, and exhibits pronounced size effects. Specifically, nanoindentation revealed an elastic modulus of 3.9 ± 0.5 GPa, which is significantly smaller than other candidate metallic anodes, e.g., Li and Mg. Furthermore, we have shown that Na metal is both softer (indentation hardness less than 1/3 that of Li at indentation depth of 10 μm) and more prone to creep than Li metal. In addition, bulk, microscale, and nanoscale testing reveal Na's marked size- and strain-rate-dependent plastic response. This strain-rate sensitivity suggests that mechanics may play a role in the deposition morphology: different morphologies may form at different deposition (i.e., strain) rates. Furthermore, the soft nature of the Na metal may play a positive role in maintaining uniform deposit morphology and in maintaining anode–SSE contact. Toward this end, Na metal's relatively low flow stress and propensity to creep (compared to Li) should have significant implications for maintaining interfacial contact at high current densities. However, Na's extremely soft and creep-prone behavior may also exacerbate other failure modes (e.g., potentially leading to the transport of Na into SSE grain boundaries, which could precipitate fracture of the SSE). Overall, the results presented here provide general reference values for mechanical properties of Na metal and can help guide the design of battery architectures and charging conditions toward reversible sodium metal batteries.

ASSOCIATED CONTENT

Supporting Information

The Supporting Information is available free of charge at <https://pubs.acs.org/doi/10.1021/acsaem.9b02225>.

Figures S1–S9 (PDF)

AUTHOR INFORMATION

Corresponding Author

Matt Pharr – Department of Mechanical Engineering, Texas A&M University, College Station, Texas 77840, United States; orcid.org/0000-0001-8738-5393; Email: m-pharr@tamu.edu

Authors

Cole D. Fincher – Department of Mechanical Engineering, Texas A&M University, College Station, Texas 77840, United States

Yuwei Zhang – Department of Mechanical Engineering, Texas A&M University, College Station, Texas 77840, United States

George M. Pharr – Department of Materials Science and Engineering, Texas A&M University, College Station, Texas 77840, United States

Complete contact information is available at: <https://pubs.acs.org/doi/10.1021/acsaem.9b02225>

Notes

The authors declare no competing financial interest.

ACKNOWLEDGMENTS

C.D.F. acknowledges the support of the National Science Foundation Graduate Research Fellowship under grant 1746932. M.P. and Y.Z. acknowledge funding from the

Mechanical Engineering Department at Texas A&M University and the Texas A&M Engineering Experimentation Station (TEES). G.M.P.'s contributions to this work were supported in part by the National Science Foundation under Grant DMR-1743343.

REFERENCES

- (1) Zheng, X.; Bommier, C.; Luo, W.; Jiang, L.; Hao, Y.; Huang, Y. Sodium metal anodes for room-temperature sodium-ion batteries: Applications, challenges and solutions. *Energy Storage Mater.* **2019**, *16*, 6–23.
- (2) Anderson, D. L. Chemical composition of the mantle. *J. Geophys. Res.* **1983**, *88* (S01), B41–B52.
- (3) Jamesh, M. I.; Prakash, A. Advancement of technology towards developing Na-ion batteries. *J. Power Sources* **2018**, *378*, 268–300.
- (4) Kim, Y.; Ha, K. H.; Oh, S. M.; Lee, K. T. High-Capacity Anode Materials for Sodium-Ion Batteries. *Chem. - Eur. J.* **2014**, *20* (38), 11980–11992.
- (5) Eftekhari, A.; Kim, D.-W. Sodium-ion batteries: new opportunities beyond energy storage by lithium. *J. Power Sources* **2018**, *395*, 336–348.
- (6) Kim, H.; Jeong, G.; Kim, Y.-U.; Kim, J.-H.; Park, C.-M.; Sohn, H.-J. Metallic anodes for next generation secondary batteries. *Chem. Soc. Rev.* **2013**, *42* (23), 9011–9034.
- (7) Yui, Y.; Hayashi, M.; Nakamura, J. In situ microscopic observation of sodium deposition/dissolution on sodium electrode. *Sci. Rep.* **2016**, *6*, 22406.
- (8) Adelhelm, P.; Hartmann, P.; Bender, C. L.; Busche, M.; Eufinger, C.; Janek, J. From lithium to sodium: cell chemistry of room temperature sodium–air and sodium–sulfur batteries. *Beilstein J. Nanotechnol.* **2015**, *6* (1), 1016–1055.
- (9) Bieker, G.; Winter, M.; Bieker, P. Electrochemical in situ investigations of SEI and dendrite formation on the lithium metal anode. *Phys. Chem. Chem. Phys.* **2015**, *17* (14), 8670–8679.
- (10) Pfeifer, K.; Arnold, S.; Becherer, J.; Das, C.; Maibach, J.; Ehrenberg, H.; Dsoke, S. Can Metallic Sodium Electrodes Affect the Electrochemistry of Sodium-Ion Batteries? Reactivity Issues and Perspectives. *ChemSusChem* **2019**, *12*, 3312–3319.
- (11) Hong, Y.-S.; Li, N.; Chen, H.; Wang, P.; Song, W.-L.; Fang, D. In operando observation of chemical and mechanical stability of Li and Na dendrites under quasi-zero electrochemical field. *Energy Storage Mater.* **2018**, *11*, 118–126.
- (12) Zhao, N.; Li, C.; Guo, X. Long-life Na–O₂ batteries with high energy efficiency enabled by electrochemically splitting NaO₂ at a low overpotential. *Phys. Chem. Chem. Phys.* **2014**, *16* (29), 15646–15652.
- (13) Gireaud, L.; Grugeon, S.; Laruelle, S.; Yrieix, B.; Tarascon, J.-M. Lithium metal stripping/plating mechanisms studies: A metallurgical approach. *Electrochem. Commun.* **2006**, *8* (10), 1639–1649.
- (14) Wilkinson, D.; Blom, H.; Brandt, K.; Wainwright, D. Effects of physical constraints on Li cyclability. *J. Power Sources* **1991**, *36* (4), 517–527.
- (15) Hirai, T.; Yoshimatsu, I.; Yamaki, J. i. Influence of electrolyte on lithium cycling efficiency with pressurized electrode stack. *J. Electrochem. Soc.* **1994**, *141* (3), 611–614.
- (16) Tian, H.-K.; Qi, Y. Simulation of the effect of contact area loss in all-solid-state Li-Ion batteries. *J. Electrochem. Soc.* **2017**, *164* (11), E3512–E3521.
- (17) Liu, J.; Bao, Z.; Cui, Y.; Dufek, E. J.; Goodenough, J. B.; Khalifah, P.; Li, Q.; Liaw, B. Y.; Liu, P.; Manthiram, A.; et al. Pathways for practical high-energy long-cycling lithium metal batteries. *Nat. Energy* **2019**, *4*, 180.
- (18) Zhou, W.; Li, Y.; Xin, S.; Goodenough, J. B. Rechargeable sodium all-solid-state battery. *ACS Cent. Sci.* **2017**, *3* (1), 52–57.
- (19) Wang, M. J.; Choudhury, R.; Sakamoto, J. Characterizing the Li-Solid-Electrolyte Interface Dynamics as a Function of Stack Pressure and Current Density. *Joule* **2019**, *3* (9), 2165–2178.
- (20) Krauskopf, T.; Mogwitz, B.; Rosenbach, C.; Zeier, W. G.; Janek, J. Diffusion Limitation of Lithium Metal and Li–Mg Alloy Anodes on LLZO Type Solid Electrolytes as a Function of Temperature and Pressure. *Adv. Energy Mater.* **2019**, *9*, 1902568.
- (21) Krauskopf, T.; Hartmann, H.; Zeier, W. G.; Janek, J. r. Toward a Fundamental Understanding of the Lithium Metal Anode in Solid-State Batteries—An Electrochemo-Mechanical Study on the Garnet-Type Solid Electrolyte Li₆ 25AlO₁₀ 25La3Zr2O12. *ACS Appl. Mater. Interfaces* **2019**, *11* (15), 14463–14477.
- (22) Cheng, L.; Crumlin, E. J.; Chen, W.; Qiao, R.; Hou, H.; Lux, S. F.; Zorba, V.; Russo, R.; Kostecki, R.; Liu, Z.; et al. The origin of high electrolyte–electrode interfacial resistances in lithium cells containing garnet type solid electrolytes. *Phys. Chem. Chem. Phys.* **2014**, *16* (34), 18294–18300.
- (23) Ferrese, A.; Newman, J. Mechanical deformation of a lithium-metal anode due to a very stiff separator. *J. Electrochem. Soc.* **2014**, *161* (9), A1350–A1359.
- (24) Ferrese, A. J. Electrochemical Modeling of a Lithium-Metal Anode. UC Berkeley, 2013.
- (25) Pharr, M.; Zhao, K.; Wang, X.; Suo, Z.; Vlassak, J. J. Kinetics of initial lithiation of crystalline silicon electrodes of lithium-ion batteries. *Nano Lett.* **2012**, *12* (9), 5039–5047.
- (26) Mistry, A.; Mukherjee, P. P. Molar Volume Mismatch: A Malefactor for Irregular Metallic Electrodeposition in Solid Electrolytes. [ChemRxiv.org](https://doi.org/10.26434/chemrxiv-2019-07-01), 2019.
- (27) Monroe, C.; Newman, J. The impact of elastic deformation on deposition kinetics at lithium/polymer interfaces. *J. Electrochem. Soc.* **2005**, *152* (2), A396–A404.
- (28) Sakamoto, J. More pressure needed. *Nat. Energy* **2019**, *4* (10), 827–828.
- (29) Kasemchainan, J.; Zekoll, S.; Spencer Jolly, D.; Ning, Z.; Hartley, G.; Marrow, T.; Bruce, P. Critical stripping current leads to dendrite formation on plating in 3 lithium anode solid electrolyte cells. *Nat. Mater.* **2019**, *18*, 1105.
- (30) Spencer Jolly, D.; Ning, Z.; Darnbrough, J. E.; Kasemchainan, J.; Hartley, G. O.; Adamson, P.; Armstrong, D.; Marrow, J.; Bruce, P. G. The sodium/Na beta alumina interface: Effect of pressure on voids. *ACS Appl. Mater. Interfaces* **2020**, *12*, 678.
- (31) Zhao, C.; Liu, L.; Qi, X.; Lu, Y.; Wu, F.; Zhao, J.; Yu, Y.; Hu, Y. S.; Chen, L. Solid-state sodium batteries. *Adv. Energy Mater.* **2018**, *8* (17), 1703012.
- (32) Kim, J. J.; Yoon, K.; Park, I.; Kang, K. Progress in the Development of Sodium-Ion Solid Electrolytes. *Small Methods* **2017**, *1* (10), 1700219.
- (33) Hou, W.; Guo, X.; Shen, X.; Amine, K.; Yu, H.; Lu, J. Solid electrolytes and interfaces in all-solid-state sodium batteries: Progress and perspective. *Nano Energy* **2018**, *52*, 279.
- (34) Quimby, S.; Siegel, S. The variation of the elastic constants of crystalline sodium with temperature between 80° K and 210° K. *Phys. Rev.* **1938**, *54* (4), 293.
- (35) Daniels, W. B. Pressure variation of the elastic constants of sodium. *Phys. Rev.* **1960**, *119* (4), 1246.
- (36) Diederich, M. E.; Trivisonno, J. Temperature dependence of the elastic constants of sodium. *J. Phys. Chem. Solids* **1966**, *27* (4), 637–642.
- (37) Martinson, R. Variation of the elastic constants of sodium with temperature and pressure. *Phys. Rev.* **1969**, *178* (3), 902.
- (38) Fritsch, G.; Geipel, F.; Prasetyo, A. The elastic constants of sodium from 20 to 95° C. *J. Phys. Chem. Solids* **1973**, *34* (11), 1961–1969.
- (39) Edwards, C. The Resistance of Metals to Penetration under Impact. *J. Inst. Met.* **1918**, 61.
- (40) Herke, P. K.; Schoeck, G. Plastic Behaviour of Sodium. *Proc. 4th Int. Conf. Strength of Metals and Alloys*. **1976**, p 151.
- (41) Sargent, P.; Ashby, M. Deformation mechanism maps for alkali metals. *Scr. Metall.* **1984**, *18* (2), 145–150.
- (42) Williams, D. B. G.; Lawton, M. Drying of organic solvents: quantitative evaluation of the efficiency of several desiccants. *J. Org. Chem.* **2010**, *75* (24), 8351–8354.

- (43) Oliver, W. C.; Pharr, G. M. An improved technique for determining hardness and elastic modulus using load and displacement sensing indentation experiments. *J. Mater. Res.* **1992**, *7* (6), 1564–1583.
- (44) Pharr, G.; Oliver, W. Measurement of thin film mechanical properties using nanoindentation. *MRS Bull.* **1992**, *17* (7), 28–33.
- (45) Ginder, R. S.; Nix, W. D.; Pharr, G. M. A simple model for indentation creep. *J. Mech. Phys. Solids* **2018**, *112*, 552–562.
- (46) Oliver, W. C.; Pharr, G. M. Measurement of hardness and elastic modulus by instrumented indentation: Advances in understandings and refinements to methodology. *J. Mater. Res.* **2004**, *19* (1), 3–20.
- (47) Merle, B.; Maier-Kiener, V.; Pharr, G. M. Influence of modulus-to-hardness ratio and harmonic parameters on continuous stiffness measurement during nanoindentation. *Acta Mater.* **2017**, *134*, 167–176.
- (48) Pharr, G. M.; Herbert, E. G.; Gao, Y. The indentation size effect: a critical examination of experimental observations and mechanistic interpretations. *Annu. Rev. Mater. Res.* **2010**, *40*, 271–292.
- (49) Maier, V.; Schunk, C.; Göken, M.; Durst, K. Microstructure-dependent deformation behaviour of bcc-metals—indentation size effect and strain rate sensitivity. *Philos. Mag.* **2015**, *95* (16–18), 1766–1779.
- (50) Fincher, C. D.; Ojeda, D.; Zhang, Y.; Pharr, G. M.; Pharr, M. Mechanical properties of metallic lithium: from nano to bulk scales. *Acta Mater.* **2020**, *186*, 215–222.
- (51) Hashin, Z.; Shtrikman, S. A variational approach to the theory of the elastic behaviour of polycrystals. *J. Mech. Phys. Solids* **1962**, *10* (4), 343–352.
- (52) Davidson, R.; Verma, A.; Santos, D.; Hao, F.; Fincher, C.; Xiang, S.; Van Buskirk, J.; Xie, K.; Pharr, M.; Mukherjee, P. P.; Banerjee, S. Formation of magnesium dendrites during electrodeposition. *ACS Energy Lett.* **2019**, *4* (2), 375–376.
- (53) Tabor, D. *The Hardness of Metals*; Oxford University Press: 2000.
- (54) Masias, A.; Felten, N.; Garcia-Mendez, R.; Wolfenstine, J.; Sakamoto, J. Elastic, plastic, and creep mechanical properties of lithium metal. *J. Mater. Sci.* **2019**, *54* (3), 2585–2600.
- (55) LePage, W. S.; Chen, Y.; Kazyak, E.; Chen, K.-H.; Sanchez, A. J.; Poli, A.; Arruda, E. M.; Thouless, M.; Dasgupta, N. P. Lithium Mechanics: Roles of Strain Rate and Temperature and Implications for Lithium Metal Batteries. *J. Electrochem. Soc.* **2019**, *166* (2), A89–A97.
- (56) Lin, D.; Liu, Y.; Li, Y.; Li, Y.; Pei, A.; Xie, J.; Huang, W.; Cui, Y. Fast galvanic lithium corrosion involving a Kirkendall-type mechanism. *Nat. Chem.* **2019**, *11* (4), 382.
- (57) Laresgoiti, I.; Käbitz, S.; Ecker, M.; Sauer, D. U. Modeling mechanical degradation in lithium ion batteries during cycling: Solid electrolyte interphase fracture. *J. Power Sources* **2015**, *300*, 112–122.
- (58) Lee, J. S.; Tai Kim, S.; Cao, R.; Choi, N. S.; Liu, M.; Lee, K. T.; Cho, J. Metal–air batteries with high energy density: Li–air versus Zn–air. *Adv. Energy Mater.* **2011**, *1* (1), 34–50.
- (59) Brissot, C.; Rosso, M.; Chazalviel, J.-N.; Baudry, P.; Lascaud, S. In situ study of dendritic growth in lithium/PEO-salt/lithium cells. *Electrochim. Acta* **1998**, *43* (10–11), 1569–1574.
- (60) Dollé, M.; Sannier, L.; Beaudoin, B.; Trentin, M.; Tarascon, J.-M. Live scanning electron microscope observations of dendritic growth in lithium/polymer cells. *Electrochem. Solid-State Lett.* **2002**, *5* (12), A286–A289.
- (61) Bayley, P. M.; Trease, N. M.; Grey, C. P. Insights into electrochemical sodium metal deposition as probed with in Situ ^{23}Na NMR. *J. Am. Chem. Soc.* **2016**, *138* (6), 1955–1961.
- (62) Herbert, E. G.; Dudney, N. J.; Rochow, M.; Thole, V.; Hackney, S. A. On the mechanisms of stress relaxation and intensification at the lithium/solid-state electrolyte interface. *J. Mater. Res.* **2019**, *34* (21), 3593–3616.
- (63) Cogswell, D. A. Quantitative phase-field modeling of dendritic electrodeposition. *Phys. Rev. E* **2015**, *92* (1), No. 011301.
- (64) Barton, J.; Bockris, J. O. M. The electrolytic growth of dendrites from ionic solutions. *Proc. R. Soc. A* **1962**, *268* (1335), 485–505.
- (65) Diggle, J.; Despic, A.; Bockris, J. M. The mechanism of the dendritic electrocrystallization of zinc. *J. Electrochem. Soc.* **1969**, *116* (11), 1503–1514.
- (66) Crowther, O.; West, A. C. Effect of electrolyte composition on lithium dendrite growth. *J. Electrochem. Soc.* **2008**, *155* (11), A806–A811.
- (67) Oren, Y.; Landau, U. Growth of zinc dendrites in acidic zinc chloride solutions. *Electrochim. Acta* **1982**, *27* (6), 739–748.
- (68) Akolkar, R. Mathematical model of the dendritic growth during lithium electrodeposition. *J. Power Sources* **2013**, *232*, 23–28.
- (69) Porz, L.; Swamy, T.; Sheldon, B. W.; Rettenwander, D.; Frömling, T.; Thaman, H. L.; Berendts, S.; Uecker, R.; Carter, W. C.; Chiang, Y. M. Mechanism of lithium metal penetration through inorganic solid electrolytes. *Adv. Energy Mater.* **2017**, *7* (20), 1701003.
- (70) Taylor, N. J.; Stangeland-Molo, S.; Haslam, C. G.; Sharafi, A.; Thompson, T.; Wang, M.; Garcia-Mendez, R.; Sakamoto, J. Demonstration of high current densities and extended cycling in the garnet $\text{Li}_7\text{La}_3\text{Zr}_2\text{O}_{12}$ solid electrolyte. *J. Power Sources* **2018**, *396*, 314–318.
- (71) Pan, H.; Hu, Y.-S.; Chen, L. Room-temperature stationary sodium-ion batteries for large-scale electric energy storage. *Energy Environ. Sci.* **2013**, *6* (8), 2338–2360.
- (72) Hao, F.; Han, F.; Liang, Y.; Wang, C.; Yao, Y. Architectural design and fabrication approaches for solid-state batteries. *MRS Bull.* **2018**, *43* (10), 775–781.
- (73) Cheng, E. J.; Sharafi, A.; Sakamoto, J. Intergranular Li metal propagation through polycrystalline $\text{Li}_6\text{Zr}_2\text{Al}_2\text{O}_{12}$ ceramic electrolyte. *Electrochim. Acta* **2017**, *223*, 85–91.
- (74) Sakuda, A.; Hayashi, A.; Tatsumisago, M. Sulfide solid electrolyte with favorable mechanical property for all-solid-state lithium battery. *Sci. Rep.* **2013**, *3*, 2261.
- (75) Manalastas, W., Jr.; Rikarte, J.; Chater, R. J.; Brugge, R.; Aguadero, A.; Buannic, L.; Llordés, A.; Aguesse, F.; Kilner, J. Mechanical failure of garnet electrolytes during Li electrodeposition observed by in-operando microscopy. *J. Power Sources* **2019**, *412*, 287–293.
- (76) Bay, M. C.; Wang, M.; Grissa, R.; Heinz, M. V.; Sakamoto, J.; Battaglia, C. Sodium Plating from $\text{Na-}\beta''\text{-Alumina}$ Ceramics at Room Temperature, Paving the Way for Fast-Charging All-Solid-State Batteries. *Adv. Energy Mater.* **2020**, *10*, No. 1902899.
- (77) Wang, M.; Wolfenstine, J. B.; Sakamoto, J. Temperature dependent flux balance of the $\text{Li/Li}_7\text{La}_3\text{Zr}_2\text{O}_{12}$ interface. *Electrochim. Acta* **2019**, *296*, 842–847.